

A UNIFIED INELASTIC CONSTITUTIVE MODEL FOR THE AVERAGE ENGINEERING RESPONSE OF GRADE 91 STEEL

M. C. Messner

Argonne National Laboratory
Lemont, Illinois, USA

V.-T. Phan

Argonne National Laboratory
Lemont, Illinois, USA

T.-L. Sham

Argonne National Laboratory
Lemont, Illinois, USA

ABSTRACT

Grade 91 steel has been called out for use in advanced reactor intermediate heat exchangers and other components. The material has good high temperature creep resistance and thermal properties but has a complex microstructure that manifests as cyclic softening, work softening, and tension/compression asymmetry in its engineering mechanical response. We describe a unified viscoplastic model for the deformation of Grade 91 for an expected operating temperature range spanning from room temperature to approximately 650°C. The model transitions from a rate independent response at low temperatures and high strain rates to a rate dependent, unified viscoplastic response at high temperatures and low creep strain rates. The model captures work and cyclic softening in the material through combined isotropic-kinematic hardening and captures observed tension/compression asymmetry and related anomalous ratcheting effects through a non- J_2 flow term. A particular focus of the model is on capturing the average response of Grade 91 as determined from a wide collection of experimental data at many different temperatures, rather than the response of a single set of experiments at a particular temperature. The final model is suitable for the engineering design of nuclear components via inelastic analysis using the ASME Section III, Division 5 procedures.

1 Introduction

This paper describes work on developing an inelastic constitutive model for Grade 91 steel. Grade 91 is an ferritic-martensitic steel with good high temperature creep resistance. However, its macroscale deformation has several anomalous features caused by its complex microstructure: cyclic softening,

work softening at elevated temperatures, tension/compression asymmetry, anomalous ratcheting, and rate dependent deformation at relatively low temperatures. A unified viscoplastic material model for Grade 91 that captures all these features is required to apply the ASME Section III, Division 5, Subsection HB, Subpart B design by inelastic analysis method. Several previous authors have developed such material models, [1,2]. This work builds on these previous models but focuses particularly on systematically capturing average material behavior by fitting to data from many different experimental programs, product forms – plate, bar, tube, and forgings – and many different batches of material. The goal is to create a model suitable for general Code use, not one that exactly matches the response of a particular batch of material.

The Code does not specify any required or recommended forms for the material model or the calibrated material constants. However, it does give some general guidance. The constitutive model must represent:

1. temperature-dependent plastic hardening or softening;
2. primary creep and the effects of creep strain hardening and softening due to reverse loading;
3. the effect of prior creep on subsequent plasticity and vice versa.

Additionally, for Grade 91 the Code strongly recommends the use of a unified viscoplastic model – a model that unifies the treatment of creep and plasticity.

The model developed here starts from a method based on Kocks-Mecking [3–5] diagrams developed to capture the material rate sensitivity and the transition from a rate sensitive to an insensitive response. This model is described in greater detail by

the authors in an upcoming publication. The hardening model starts from the standard form developed by Chaboche to represent cyclic plasticity [6–12]. It adds dynamic recovery terms to the backstress formulation to account for the time-dependent interaction of creep and plasticity. The standard Voce isotropic hardening model is inverted into isotropic softening to represent cyclic softening, work softening, and tertiary creep. The model uses a non- J_2 flow rule to account for tension/compression asymmetry and anomalous ratcheting. The parameters of this general model are calibrated against a large experimental dataset collected from the literature. The calibration scheme has three stages: first manual calibration, then calibration with a large, parallel genetic algorithm, and finally by fine tuning with local, gradient-free optimization schemes. The final model well-represents the average response of Grade 91 across a large temperature range – room temperature to 650°C – as well as capturing the behavior of validation experiments.

Section 2 describes the model and the experimental database. Section 3 describes the optimization approaches used to derive the model parameters. Section 4 compares the model to both the average material response – including data scatter due to processing and batch variation – and to several specific validation experiments. Finally, Section 5 summarizes the lessons learned in the model development and calibration process and how they could be applied to calibrating material models for the remainder of the Section III, Division 5 Class A materials.

2 Model form and experimental database

2.1 The unified viscoplastic model

The overall material model is a time integration of the strain rate decomposition

$$\dot{\epsilon} = \dot{\epsilon}_e + \dot{\epsilon}_p + \dot{\epsilon}_{th} \quad (1)$$

with

$$\dot{\epsilon}_e = \mathbf{C}^{-1} : \dot{\sigma}, \quad (2)$$

$$\dot{\epsilon}_{th} = \alpha \dot{T} \mathbf{I} \quad (3)$$

where \mathbf{C} is an isotropic, temperature dependent elasticity tensor calculated using the constants in Section II of the ASME Code and α is the temperature dependent instantaneous coefficient of thermal expansion, again from the Section II Code values. This equation is implemented as a numerical integration for the stress, i.e.

$$\dot{\sigma} = \mathbf{C} : (\dot{\epsilon} - \dot{\epsilon}_p - \dot{\epsilon}_{th}). \quad (4)$$

Given the constant strain rate $\dot{\epsilon}_{n+1}$ over a time step Δt_{n+1} and the temperature at the next step T_{n+1} the model returns the updated stress σ_{n+1} and a set of internal variables integrated from the ordinary differential equation

$$\dot{h} = r(\sigma, h). \quad (5)$$

The model for material rate sensitivity switches from a rate sensitive response to an insensitive response as the temperature and strain rate of deformation changes. An upcoming publication by the authors describes the method in greater detail. The basic idea is to construct a Kocks-Mecking diagram [3–5, 13, 14] and model the rate sensitivity of the material on regions in the diagram. Figure 1 shows a Kocks-Mecking diagram for Grade 91 steel. The x-axis of these diagrams is a nondimensional normalized activation energy

$$g = \frac{kT}{\mu b^3} \log \left(\frac{\dot{\epsilon}_0}{\dot{\epsilon}} \right) \quad (6)$$

where k is the Boltzmann constant, T the absolute temperature, μ the temperature-dependent shear modulus, b the Burgers vector, $\dot{\epsilon}_0$ a reference strain rate, here $\dot{\epsilon}_0 = 10^{10} \text{ s}^{-1}$, and $\dot{\epsilon}$ the deformation strain rate. This work uses log for the natural logarithm. The y-axis of the diagram plots the logarithm of the corresponding flow stress normalized by the temperature-dependent shear modulus. This Kocks-Mecking diagram plots data from uniaxial tension, creep, and stress relaxation tests. For uniaxial tension tests the strain rate and temperature are controlled and the figure plots the experimental yield stress. For a creep tests the temperature and flow stress are controlled and the diagram plots the initial primary creep rate. Using the yield stress and the initial rate of primary creep avoids the influence of work softening on the material rate sensitivity. Each stress relaxation experiment yields a line of the Kocks-Mecking diagram plotted with 10 discrete points on the diagram. Stress relaxation tests are at a fixed temperature. The results are summarized in a stress relaxation plot of stress versus time. Each point on the Kocks-Mecking line corresponds to a single time on the stress relaxation curve. The curve gives the flow stress directly. The strain rate is calculated based on the decomposition of strain at fixed, constant strain

$$\dot{\epsilon} = 0 = \dot{\epsilon}_e + \dot{\epsilon}_p = \frac{\dot{\sigma}}{E} + \dot{\epsilon}_p \quad (7)$$

$$\dot{\epsilon}_p = -\frac{\dot{\sigma}}{E} \quad (8)$$

where the relaxation rate $\dot{\sigma}$ can be calculated by numerically differentiating the stress relaxation profile.

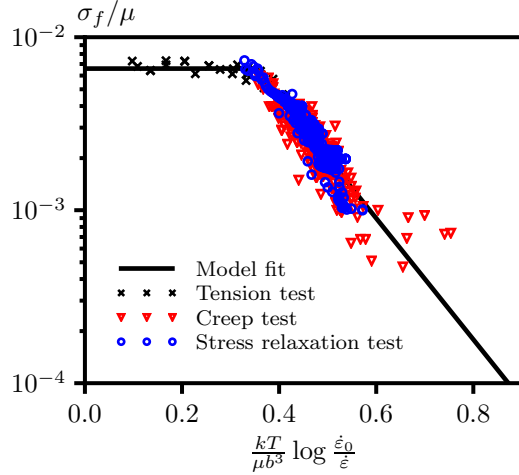


FIGURE 1. Kocks Mecking diagram for Grade 91. The points represent individual experiments and the solid line is the bilinear relation used in the model for rate sensitivity.

Figure 1 shows that the Kocks-Mecking diagram has a bilinear form with an initial, flat portion followed by a steep, linear drop off. The initial flat section of the curve is the region of rate insensitivity while the sloped portion is the region of rate sensitive deformation. The bilinear curve sets the model rate sensitivity. Let g_0 be the knee of the curve in terms of the normalized activation energy, let A and B be the slope and intercept of the rate sensitive region, and let C be the constant normalized flow stress of the rate insensitive region. Note that $B = C - Ag_0$. A standard material model embedded in a finite element solver is strain controlled. At the start of a time step the model knows the step strain rate and temperature. From these, the model calculates the normalized activation energy for the step, g_{n+1} , using Eq. 6. If $g_{n+1} < g_0$ then the model will take a rate independent, associative step

$$\dot{\epsilon}^p = \gamma \frac{\partial f}{\partial \sigma} \quad (9)$$

$$\gamma \geq 0 \quad (10)$$

$$f(\sigma) \leq 0 \quad (11)$$

$$\gamma f(\sigma) = 0 \quad (12)$$

$$\gamma \dot{f}(\sigma) = 0 \quad (13)$$

for

$$f(\sigma) = L(\sigma) - \sqrt{\frac{2}{3}} \sigma_f \quad (14)$$

$$\sigma_f = \sigma_0 + \sigma_{iso} \quad (15)$$

with the yield stress

$$\sigma_0 = \mu e^C. \quad (16)$$

The function $L(\sigma)$ and the form of the isotropic hardening are described below. Even in the rate insensitive region the model flow stress is still temperature dependent through the shear modulus.

If $g \geq g_0$ then the model takes a rate dependent step with the power law viscoplastic model

$$\dot{\epsilon}^p = \gamma \frac{\partial f}{\partial \sigma} \quad (17)$$

$$\dot{\gamma} = \left\langle \frac{\left(L(\sigma) - \sqrt{\frac{2}{3}} \sigma_f \right)^n}{\eta} \right\rangle \quad (18)$$

$$\sigma_f = \sigma_{iso} \quad (19)$$

$$n = -\frac{\mu b^3}{kTA} \quad (20)$$

$$\eta = e^B \mu \dot{\epsilon}_0^{kTA/(\mu b^3)} \quad (21)$$

where $\langle \rangle$ are the Macaulay brackets.

For reasons described in greater detail below the model uses a non- J_2 flow rule

$$L(\sigma) = \|\mathbf{s} - \mathbf{X}\| - h \text{sign}(p) p^l$$

where \mathbf{s} is the deviatoric stress, \mathbf{X} the backstress, $p = \text{tr}(\sigma)$, and h and l are temperature dependent material properties. This form was proposed by Yaguchi [15] to represent tension/compression asymmetry and anomalous ratcheting in Grade 91.

The isotropic hardening σ_{iso} has a Voce form

$$\sigma_{iso} = R(1 - \exp(-\delta \bar{\epsilon}_p)) \quad (22)$$

with R and δ temperature dependent parameters and $\bar{\epsilon}_p$ an internal variable defined with

$$\dot{\bar{\epsilon}}_p = \dot{\gamma}. \quad (23)$$

For Grade 91 the Voce model will be used represent softening with the saturation stress $R < 0$.

Finally, the backstress takes the full Chaboche form includ-

ing static and dynamic recovery:

$$\mathbf{X} = \sum_{i=1}^n \mathbf{X}_i \quad (24)$$

$$\dot{\mathbf{X}}_i = \left(\frac{2}{3} C_i \frac{\partial f}{\partial \boldsymbol{\sigma}} - \sqrt{\frac{2}{3}} \gamma_i \mathbf{X}_i \right) \dot{\gamma} - A_i \sqrt{\frac{3}{2}} \|\mathbf{X}_i\|^{a_i-1} \quad (25)$$

with C_i , γ_i , A_i , and a_i all temperature dependent material constants. Here n is the number of backstresses used in the model. The current work uses $n = 2$.

These equations fully define the constitutive model at a fixed temperature. Defining the model for a particular temperature requires 15 material constants, not counting the elastic and thermal properties. The model captures the temperature dependence of the properties by defining a set of temperature control points at 25, 400, 500, 550, 600, and 650° C. The model constants are defined at these temperatures. In between these control points the model constants are linearly interpolated.

2.2 Experimental data

The model constants are set by optimizing against a large database of experiments. Table 1 lists the sources of the experimental data used to calibrate the model. The database includes five general kinds of experiments: uniaxial tension, creep, stress relaxation, strain controlled cyclic, and stress controlled cyclic. Many of the cyclic experiments include strain or stress holds. Overall the database contains data from 463 individual experiments.

3 Calibrating the model

The model optimization process has several steps. First, an initial guess for the model parameters is set manually by running simulations and comparing them to the experimental data. The second step uses a genetic algorithm (GA) to optimize the model. The objective function is the sum of the integrated difference between the simulation and the experimental stress/strain curves for each experiment in the database. For example, for a uniaxial tension test the data is a stress/strain curve. The optimizer simulates a tension curve under the experimental conditions and the computes the difference

$$e = \int_0^{\epsilon_{max}} |\sigma_{exp}(\epsilon) - \sigma_{model}(\epsilon)| d\epsilon \quad (26)$$

where ϵ_{max} is the maximum strain recorded in the experiment. For cyclic tests the compared curves are the maximum, mean, or minimum stress versus cycle data to avoid integrating through the full stress/strain history. The error for each experiment has

a weight factor applied and all the weighted errors are summed into a single scalar value representing how well the model represents the experimental database. The weight factors are set to approximately equally weigh each class of experiments. So, for example, if there are m experiments in the database for a type of experiment then the weight factor will be $1/m$.

The genetic algorithm uses the opposite of this total error as the fitness function, i.e. it poses the fit as a maximization problem. The algorithm starts with an initial population of models as represented by the model parameters. This initial population includes the manually calibrated guess, random permutations of the manual guess, and completely random parameter sets. The GA evolves this initial population to maximize the total fitness (minimize the total error) by applying standard selection, crossover, and mutation methods. Each iteration of the GA produces a new population with a better average and maximum fitness. This process repeats until the fitness score stabilizes. The GA used here has a population of 75 members. To reduce the time required to evaluate the fitness of each member, which requires $75 \times 463 = 34,725$ individual simulations, each of which can be lengthy, the algorithm carries out the simulations in parallel over 1600 individual processes on a cluster. The implementation uses MPI to communicate data and results between processes. Typically the optimization requires over 1 week of wall time to stabilize which represents about 300,000 CPU-hours of work. This GA is implemented using the DEAP python framework [26].

The model with the highest fitness at the end of the last iteration of the algorithm is extracted from the GA output and used as a candidate for the final model. Model parameters were altered slightly from the GA output to reduce the number of significant figures. This did not significantly affect model accuracy.

The model calibration includes the temperature interpolation scheme. Many of the experiments in the database were not conducted at one of the temperature control points. This means the corresponding simulations use the interpolated material properties to try to match the experimental data. The model as a whole, including the interpolation scheme, is evolved towards a global optima. This is a different approach than calibrating the model at several temperatures and then later interpolating between the calibration points.

Tables 2 and 3 lists the model parameters for the final version of the Grade 91 inelastic model. In total there are 72 material constants plus the definition of the temperature dependent elastic properties and the coefficient of thermal expansion.

4 Results

4.1 General response

Figure 2 plots the model's response for uniaxial tension at (a) a fixed strain rate and increasing temperatures and (b) a constant temperature but increasing strain rate. Subfigure (a) shows that the model remains temperature dependent at low temper-

Source	Test types
Asayama and Tachibana [16]	Creep, stress relaxation
Choudhary and Isaac Samuel [17]	Creep
Kim and Weertman [18]	Monotonic, cyclic
Kimura, Kushima, and Sawada [19]	Creep
Koo, Lee, and Kwon [2, 20]	Cyclic, stress relaxation
Latha et al. [21]	Monotonic, creep
Maruyama et al. [22]	Creep
Swindeman [23]	Monotonic
Yaguchi and Takahashi [1, 15, 24]	Monotonic, stress relaxation, cyclic
Zhang and Aktaa [25]	Cyclic
Archived DOE reports	All types of experiments

TABLE 1. Summary of data sources for Gr. 91 steel.

Parameter	Units	25° C	400° C	500° C	550° C	600° C	650° C
h	-	2×10^{-4}	2×10^{-4}	2×10^{-4}	2×10^{-4}	2×10^{-4}	2×10^{-4}
l	-	1.91	1.91	1.71	1.69	1.61	1.51
R	MPa	-96	-96	-150	-151	-151	-131
δ	-	2.00	1.71	1.71	1.51	1.51	1.00
C_1	MPa	14500	15000	19000	19200	19900	19000
γ_1	-	141	141	802	792	803	803
A_1	MPa^{1-a_1}	1×10^{-15}	1×10^{-15}	1×10^{-15}	1×10^{-15}	1×10^{-15}	1×10^{-15}
a_1	-	3.5	3.5	5.97	5.97	7.47	9.46
C_2	MPa	12500	12500	12500	12600	12400	12400
γ_2	-	60.6	60.4	200	200	202	202
A_2	MPa^{1-a_2}	1×10^{-15}	1×10^{-15}	1×10^{-15}	1×10^{-15}	1×10^{-15}	1×10^{-15}
a_2	-	3.5	3.5	5.96	5.96	7.51	9.53

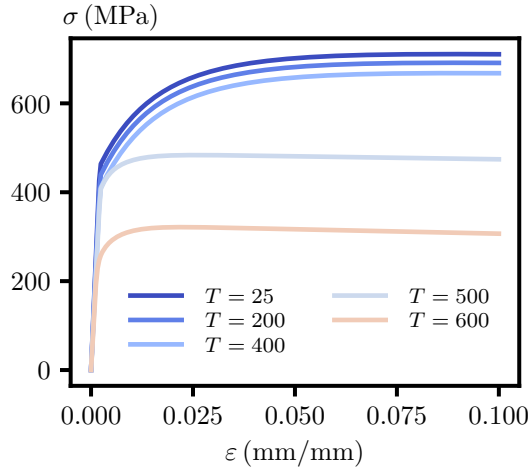
TABLE 3. Model rate sensitivity parameters.

Parameter	Value
A	-9.698
C	-5.119
g_0	0.3496

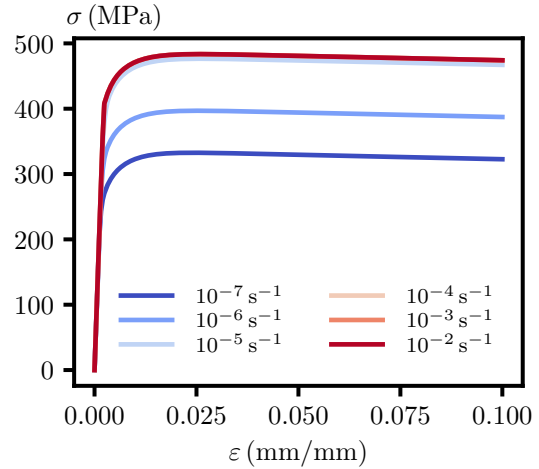
TABLE 2. Model rate sensitivity parameters. Parameters are unitless.

atures in the rate independent regime because the yield stress scales with the temperature dependent shear modulus. Subfigure (b) illustrates the ability of the model to switch from a rate dependent to a rate independent response. As the strain rate increases the flow curves coalesce as the model transitions into the rate independent regime.

Figures 1 and 3 illustrate the difficulty inherent in trying to calibrate an inelastic model to the average response of many material batches and product forms instead of to a particular, limited



a)



b)

FIGURE 2. (a) Temperature dependence of the uniaxial tension flow curve for a strain rate of $\dot{\epsilon} = 8.33 \times 10^{-5} \text{ s}^{-1}$ – the rate specified by the ASTM E21 standard. (b) Strain rate dependence of the uniaxial flow curve at $T = 500^\circ \text{C}$.

set of experimental data on a single batch. Figure 1 is the Kocks-Mecking diagram. This diagram summarizes a large amount of experimental data: uniaxial tension, stress relaxation, and creep tests. It shows that, particularly in the creep regime, there are very large material variations from one test to another and from one batch of material to another. The model attempts to match the average material rate sensitivity. However, this means for any comparison to a particular experimental result, e.g. a particular creep test, there could be a large difference between the particular material used in the test and the average response. This does not imply that the model form is deficient, but rather it is just a consequence of the large scatter in the experimentally observed response.

Figure 3 emphasizes this point. This figure compares the model yield stress to part of yield stress data used to calculate the values for S_y in Section II of the ASME Code. These tests are at fixed strain rate but different temperatures. For a given temperature different batches of material and different product the yield stress varies by 20 to 100%. This trend might be extrapolated to the model results in general: in comparison to any particular experiment the model response might have a similar variability simply due to batch-to-batch and product form variation. The key point for a model intended for use with the Section III, Division 5, Subsection HB, Subpart B design by inelastic analysis provisions is that the model must capture the average response of the material, considering batch and product form variation. The model proposed here does this by considering a large experimental database collected from many different sources. This is in contrast to many previous models for Grade 91 which consider only a set of experiments conducted on a single batch of

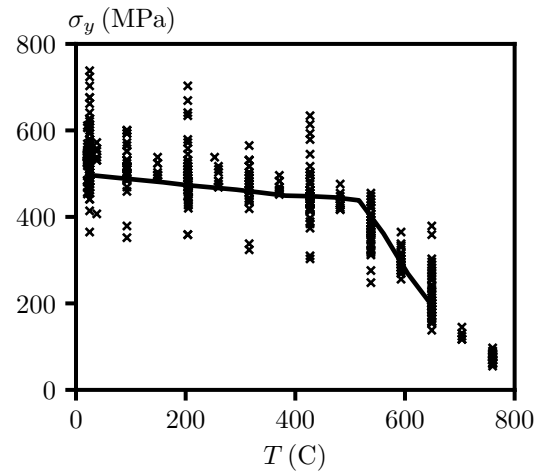
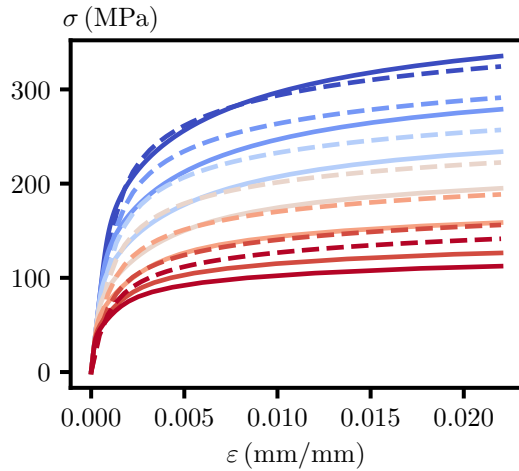
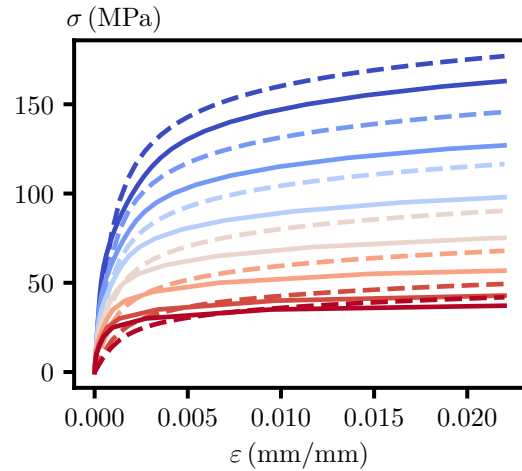


FIGURE 3. Plot comparing the yield stress as a function of temperature for rate of $\dot{\epsilon} = 8.33 \times 10^{-5} \text{ s}^{-1}$ for the model (solid line) and part of the experimental data underlying the Section II Code values of S_y for Grade 91.

material at a single test facility. Additionally, the calibration procedure tries to ensure that the final model parameters reflect a rigorous best fit to the experimental database as a whole. This is an improvement over manual model calibration, which relies on the judgment of the person doing the calibration. There are flaws in the calibration processes described above. For example, there is no guarantee that the GA optimization process will find a true global minima. However, the automated calibration used here at least systematizes the process of developing material con-

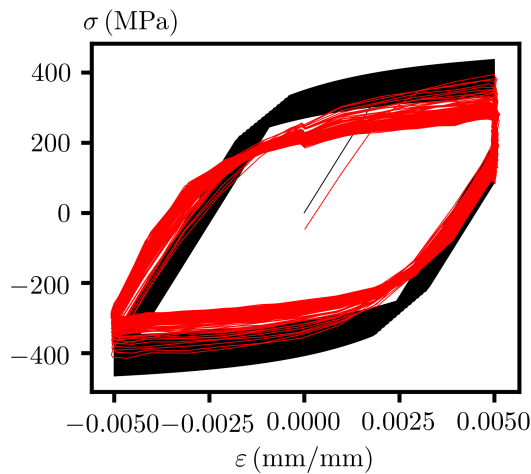


a)

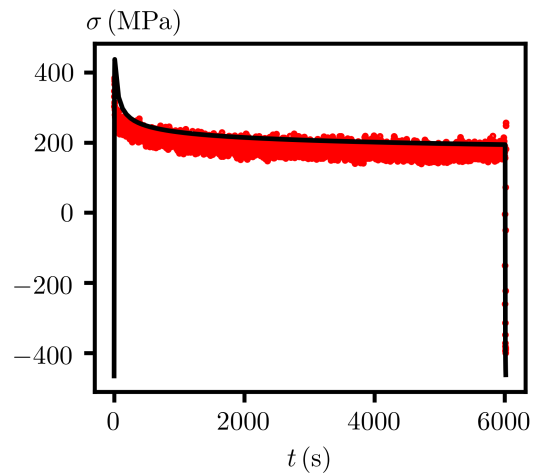


b)

FIGURE 4. These figures compare simulated isochronous curves (solid lines) to the curves described in the Code (dashed lines). The colors, from blue to red, and the curves, from top to bottom, represent lives of 1, 10, 100, 1,000, 10,000, 100,000, and 300,000 hours. Subfigure (a) shows results for $T = 550^{\circ}\text{C}$ and (b) shows results for $T = 650^{\circ}\text{C}$.



a)



b)

FIGURE 5. This figure compares the model to an experimental creep-fatigue test. (a) shows the hysteresis loops from the experiment and the corresponding simulation and (b) shows the stress relaxation profile over the second cycle of the experiment and simulation. Simulation results are in black and experimental results are in red.

stants and ensures the constants well represent the average of the collected experimental data.

4.2 Comparison to specific design curves and experiments

This section compares the model to a series of validation experiments. None of the experimental data referenced in this section was used in the model calibration.

Figure 4 compares the ASME Section III, Division 5 isochronous curves to corresponding simulated curves using the inelastic model. The Code curves nominally represent the average creep response of Grade 91 [27]. The simulated isochronous curves are created from the results of many creep simulations at different temperatures and stress levels. The Code curves and the model curves are similar, particularly in light of the large test-to-test and heat-to-heat variation in creep testing. This comparison

demonstrates the inelastic model captures the average creep response of Grade 91.

Figure 5 shows a detailed comparison to a creep-fatigue test conducted at Argonne National Laboratory. The results of this particular creep-fatigue were not included in the fit database, meaning this is a fair validation comparison. The test cycled the specimen under fully-reversed strain controlled loading with a $\Delta\epsilon = 0.5\%$ at a strain rate of $\dot{\epsilon} = 10^{-3} \text{ s}^{-1}$ at $T = 550^\circ \text{ C}$ with a hold of $t = 100 \text{ min}$ on the tension side of the cycle. Figure 5a compares the model and experimental stress-strain hysteresis loops. The model captures the trends in the cyclic experiment, particularly the development of cyclic softening. The main discrepancy between the model and the experiment is in the initial flow stress which, as shown in Fig. 3, has high batch-to-batch variation. Figure 5b shows the stress relaxation profile during the tensile hold during the second cycle. Again, the model and the experiment are consistent with the main difference between the two being the initial flow stress.

Figures 6 and 7 compare the model to two ASTM E2368 - 10 standard strain-controlled thermomechanical tests conducted at Oak Ridge National Laboratory. These particular tests impose zero mechanical strain, all the strain comes from fully reversed thermal cycling. For the test summarized in Fig. 6 the specimen temperature cycles between 500° C and 600° C at a rate of 10° C/min . For the test in Fig. 7 the temperature cycles between 150° C and 650° C at a rate of 10° C/min . Again, as expected, the tests and simulations do not perfectly correspond. However, the model correctly captures the experimental trends, including the development of cyclic hardening and softening.

Finally, Fig. 8 compares the model to a series of stress controlled cyclic experiments, sourced from [24]. All these tests were at a temperature of 550° C , have a maximum stress of $\sigma_{max} = 400 \text{ MPa}$, and a stress rate of $\dot{\sigma} = 50 \text{ MPa/s}$. Each test has a different stress ratio $R = \sigma_{min}/\sigma_{max}$, labeled on the diagram. The experimental data, shown with solid lines exhibits anomalous ratcheting. For fully reversed loading and even for loading with a slightly higher maximum compressive stress than maximum tensile stress the material develops tensile ratcheting strains. This is unexpected for a material that obeys a standard J_2 flow rule. The dashed lines show the model response under corresponding loading conditions. The model obeys the general trend of the experimental data: the loading with stress ratios $R = -1.0$ and $R = -1.025$ ratchet in the tensile direction. The model can capture this trend because it uses a non- J_2 flow rule proposed by Yaguchi and Takahashi [15], designed to capture both anomalous ratcheting and tension/compression asymmetry.

These comparisons to strain controlled cyclic, stress controlled cyclic, and thermomechanical cyclic tests demonstrate that the model captures the correct trends for cyclic loading, including the effects of cyclic softening and non- J_2 flow. Overall then the proposed model captures the average material response for time-independent properties like elastic constants,

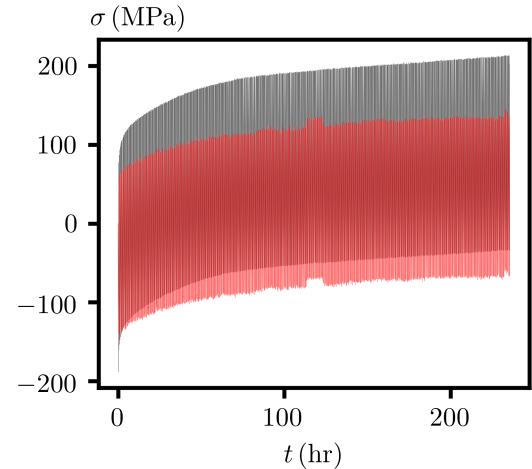


FIGURE 6. Comparison between the model and an experiment for a thermomechanical test. The figure plots the stress versus time profiles for the model (black) and experiment (red) for full constrained thermal cycling between 500° C and 600° C at a rate of 10° C/min .

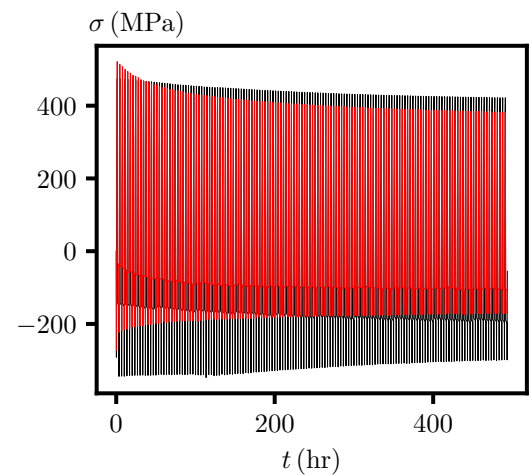


FIGURE 7. Comparison between the model and an experiment for a thermomechanical test. The figure plots the stress versus time profiles for the model (black) and experiment (red) for full constrained thermal cycling between 150° C and 650° C at a rate of 10° C/min .

rate-dependent properties like the material yield stress and uniaxial flow curves, time-dependent properties like creep, and cyclic response including cyclic softening.

5 Conclusions

This work describes an inelastic model for Grade 91 steel suitable for use with the design by inelastic analysis provisions of ASME Section III, Division 5. The model captures all rele-

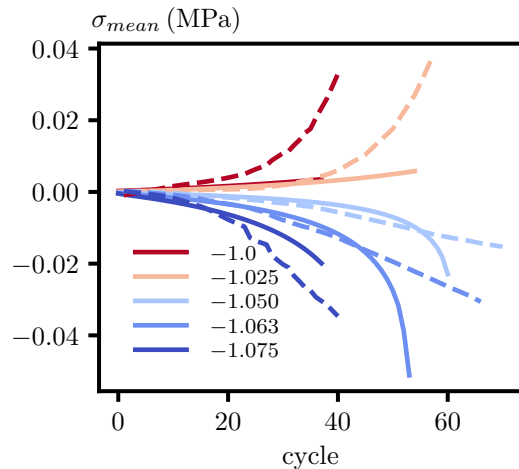


FIGURE 8. Comparison between the model (solid lines) and a stress controlled cyclic experiment (dashed lines) for the same maximum stress and several different values of stress ratio, shown on the plot.

vant deformation modes for Grade 91, including creep and cyclic behavior. The model aims to capture the average response of Grade 91, not the response of a particular batch and product form. There is considerable scatter in material property data when considering the full range of product forms and batch-to-batch material variation. The calibration procedure used to generate the model material constants ensures that the parameters are a best fit to the average of a large collection of experimental data. This approach is consistent with the Division 5 rules, which are generally applicable to all material that meets the material specification. However, one consequence of this approach is that the final constitutive model will not exactly agree with any particular experiment. Instead, a successful model must correctly capture the general experimental trend for all available experimental data and not produce physically or numerically unreasonable results. The design margin incorporated into the Code provisions ensures that a design based on the average material response will successfully bound the in-service behavior of a particular component.

Many of these lessons are applicable to the other Section III, Division 5 Class A materials. The general philosophy remains the same: the model must fit the average material response accounting for batch and production form variation. The calibration strategy developed here for Grade 91 can be applied to other materials provided sufficient experimental data can be collected from the literature.

ACKNOWLEDGMENT

The research was sponsored by the U.S. Department of Energy, under Contract No. DE-AC02-06CH11357 with Argonne National Laboratory, managed and operated by UChicago Ar-

gonne LLC. Programmatic direction was provided by the Office of Nuclear Energy.

COPYRIGHT NOTICE

This manuscript has been co-authored by UChicago Argonne LLC under Contract No. DE-AC02-06CH11357 with the U.S. Department of Energy. The United States Government retains and the publisher, by accepting the article for publication, acknowledges that the United States Government retains a nonexclusive, paid-up, irrevocable, world-wide license to publish or reproduce the published form of this manuscript, or allow others to do so, for United States Government purposes. The Department of Energy will provide public access to these results of federally sponsored research in accordance with the DOE Public Access Plan: (<http://energy.gov/downloads/doe-public-access-plan>).

REFERENCES

- [1] Yaguchi, M., and Takahashi, Y., 1999. "Unified Inelastic Constitutive Model for Modified 9Cr-1Mo Steel Incorporating Dynamic Strain Aging Effect". *JSME International Journal, Series A*, **42**(1), pp. 1–10.
- [2] Koo, G. H., and Kwon, J. H., 2011. "Identification of inelastic material parameters for modified 9Cr-1Mo steel applicable to the plastic and viscoplastic constitutive equations". *International Journal of Pressure Vessels and Piping*, **88**(1), pp. 26–33.
- [3] Kocks, U. F., 2001. "Realistic constitutive relation for metal plasticity". *Materials Science and Engineering A*, **317**, pp. 181–187.
- [4] Kocks, U. F., Argon, A. S., and Ashby, M. F., 1975. "Thermodynamics and kinetics of slip". In *Progress in Materials Science*, B. Chalmers, J. W. Christian, and T. B. Massalski, eds. pp. 64–291.
- [5] Mecking, H., Nicklas, B., Zarubova, N., and Kocks, U. F., 1986. "A "universal" temperature scale for plastic flow". *Acta Metallurgica*, **34**(3), pp. 527–535.
- [6] Chaboche, J. L., and Cailletaud, G., 1986. "On the calculation of structures in cyclic plasticity or viscoplasticity". *Computers and Structures*, **23**(1), pp. 23–31.
- [7] Chaboche, J. L., 1986. "Time-independent constitutive theories for cyclic plasticity". *International Journal of Plasticity*, **2**(2), pp. 149–188.
- [8] Chaboche, J., 1989. "Constitutive equations for cyclic plasticity and cyclic viscoplasticity". *International Journal of Plasticity*, **5**, pp. 247–302.
- [9] Chaboche, J. L., 1991. "On some modifications of kinematic hardening to improve the description of ratchetting effects". *International Journal of Plasticity*, **7**(7), pp. 661–678.

- [10] Chaboche, J. L., and Cailletaudb, G., 1996. "Integration methods for complex plastic constitutive equations". *Computational Methods in Applied Mechanics and Engineering*, **133**(95), pp. 125–155.
- [11] Chaboche, J.-L., 1997. "Thermodynamic formulation of constitutive equations and application to the viscoplasticity and viscoelasticity of metals and polymers". *International Journal of Solids and Structures*, **34**(18), pp. 2239–2254.
- [12] Chaboche, J. L., 2008. "A review of some plasticity and viscoplasticity constitutive theories". *International Journal of Plasticity*, **24**(10), oct, pp. 1642–1693.
- [13] Kocks, U. F., 1998. "Kinematics and Kinetics of Plasticity". In *Texture and Anisotropy*, U. F. Kocks, C. N. Tome, and H.-R. Wenk, eds. ch. 8, pp. 327–389.
- [14] Mecking, H., and Kocks, U. F., 1981. "Kinetics of flow and strain-hardening". *Acta Metallurgica*, **29**, pp. 1865–1875.
- [15] Yaguchi, M., and Takahashi, Y., 2005. "Ratchetting of viscoplastic material with cyclic softening, part 2: application of constitutive models". *International Journal of Plasticity*, **21**, pp. 835–860.
- [16] Asayama, T., and Tachibana, Y., 2009. Existing Evaluation Procedures for Grade 91 and Hastelloy XR. Tech. rep., ASME STP-NU-018.
- [17] Choudhary, B. K., and Isaac Samuel, E., 2011. "Creep behaviour of modified 9Cr-1Mo ferritic steel". *Journal of Nuclear Materials*, **412**(1), pp. 82–89.
- [18] Kim, S., and Weertman, J. R., 1988. "Investigation of Microstructural Changes in a Ferritic Steel Caused by High Temperature Fatigue". *Metallurgical Transactions*, **19A**(April), pp. 999–1007.
- [19] Kimura, K., Kushima, H., and Sawada, K., 2009. "Long-term creep deformation property of modified 9Cr-1Mo steel". *Materials Science and Engineering A*, **510-511**(C), pp. 58–63.
- [20] Koo, G. H., and Lee, J. H., 2007. "Investigation of ratchetting characteristics of modified 9Cr-1Mo steel by using the Chaboche constitutive model". *International Journal of Pressure Vessels and Piping*, **84**(5), pp. 284–292.
- [21] Latha, S., Nandagopal, M., Selvi, S. P., Laha, K., and Mathew, M. D., 2014. "Tensile and creep behaviour of modified 9Cr-1Mo steel cladding tube for fast reactor using metallic fuel". *Procedia Engineering*, **86**, pp. 71–79.
- [22] Maruyama, K., Nakamura, J., Yoshimi, K., and Nagae, Y., 2016. "Evaluation of long-term creep rupture life of Gr.91 steel by analysis of on-going creep curves". In *Proceedings from the Eighth International Conference on Advances in Materials Technology for Fossil Power Plants*, pp. 467–478.
- [23] Swindeman, R. W., 1988. "Cyclic Stress-Strain-Time Response of a 9Cr-1Mo-V-Nb Pressure Vessel Steel at High Temperature". In *Low Cycle Fatigue, ASTM STP 942*, H. D. Solomon, G. R. Halford, L. R. Kaisand, and B. N. Leis, eds. American Society for Testing and Materials, Philadelphia, pp. 107–122.
- [24] Yaguchi, M., and Takahashi, Y., 2005. "Ratchetting of viscoplastic material with cyclic softening, part 1: Experiments on modified 9Cr-1Mo steel". *International Journal of Plasticity*, **21**(1), pp. 43–65.
- [25] Zhang, K., and Aktaa, J., 2016. "Characterization and modeling of the ratcheting behavior of the ferritic-martensitic steel P91". *Journal of Nuclear Materials*, **472**, pp. 227–239.
- [26] Fortin, F.-A., De Rainville, F.-M., and Gardner, M.-A., 2012. "DEAP: Evolutionary algorithms made easy". *Journal of Machine Learning Research*, **13**, pp. 2171–2175.
- [27] Swindeman, R. W., 1999. "Construction of isochronous stress-strain curves for 9Cr-1Mo-V Steel". *Advances in Life Prediction Methodology*, **391**, pp. 95–100.